

# Energy-level Alignment Tuning at Tetracene/c-Si Interfaces

Jens Niederhausen<sup>1,\*</sup>, Rowan W. MacQueen<sup>1</sup>, Engin Özkol<sup>2</sup>, Clemens Gersmann<sup>1</sup>, Moritz H. Futscher<sup>3,#</sup>, Martin Liebhaber<sup>1</sup>, Dennis Friedrich<sup>4</sup>, Mario Borgwardt<sup>4</sup>, Katherine A. Mazzi<sup>5,6</sup>, Patrick Amsalem<sup>7</sup>, Minh Hai Nguyen<sup>1,6</sup>, Benjamin Daiber<sup>3</sup>, Mathias Mews<sup>2</sup>, Jörg Rappich<sup>2</sup>, Florian Ruske<sup>2</sup>, Rainer Eichberger<sup>4</sup>, Bruno Ehrler<sup>3</sup>, Klaus Lips<sup>1</sup>

<sup>1</sup>*Department Spins in Energy Conversion and Quantum Information Science (ASPIN) and Energy Materials In-Situ Laboratory Berlin (EMIL), Helmholtz-Zentrum Berlin für Materialien und Energie GmbH, 14109 Berlin, Germany*

\*E-mail: [jens.niederhausen@helmholtz-berlin.de](mailto:jens.niederhausen@helmholtz-berlin.de) Phone: +49 30 8062-1-3859

<sup>2</sup>*Institute for Silicon Photovoltaics, Helmholtz-Zentrum Berlin für Materialien und Energie GmbH, 12489 Berlin, Germany*

<sup>3</sup>*AMOLF, Center for Nanophotonics, 1098 XG Amsterdam, The Netherlands*

<sup>4</sup>*Institute for Solar Fuels, Helmholtz-Zentrum Berlin für Materialien und Energie GmbH, 14109 Berlin, Germany*

<sup>5</sup>*Joint Research Group Operando Battery Analysis, Helmholtz-Zentrum Berlin für Materialien und Energie GmbH, 12489 Berlin, Germany*

<sup>6</sup>*Department of Chemistry, Humboldt-Universität zu Berlin, 12489 Berlin, Germany*

<sup>7</sup>*Department of Physics, Humboldt-Universität zu Berlin, 12489 Berlin, Germany*

#*Current address: Laboratory for Thin Films and Photovoltaics, Empa—Swiss Federal Laboratories for Materials Science and Technology, Überlandstrasse 129, CH-8600 Dübendorf, Switzerland*

## Abstract

The rational combination of tetracene (Tc) with crystalline silicon (c-Si) could greatly enhance c-Si solar cell efficiencies via singlet fission. The Tc/c-Si energy-level alignment (ELA) is thought to be central to controlling the required interface transfer processes. We modified hydrogen-terminated c-Si (H-Si) with 2,2'-(perfluoronaphthalene-2,6-diylidene)dimalononitrile (F6TCNNQ), C<sub>60</sub>, or NF<sub>3</sub> and probed the effect on the c-Si surface chemistry, the Tc/c-Si ELA, the Tc morphology, and solar cell characteristics using ultraviolet and X-ray photoelectron spectroscopy, atomic force microscopy, X-ray diffraction, photoluminescence transients, device measurements, and transfer matrix-optical modelling.

Sub-monolayer interlayers of F6TCNNQ shifted the Tc/H-Si(111) ELA by up to 0.55 eV. C<sub>60</sub> showed no notable effect on the ELA and proved detrimental for the Tc film morphology and solar cell performance. Neither F6TCNNQ nor C<sub>60</sub> improved the Tc-related photocurrent significantly.

NF<sub>3</sub> CVD substituted the H-termination of H-Si(100) with more electronegative species and resulted in work functions as high as 6 eV. This changed the Tc/H-Si(100) ELA by up to 0.45 eV. NF<sub>3</sub> plasma from a remote source caused pronounced c-Si oxidation and a diminished c-Si photoluminescence lifetime, which was not observed for NF<sub>3</sub> plasma created in close proximity to the c-Si surface or neutral NF<sub>3</sub>.

We discuss possible reasons for why the improved ELA does not lead to an improved singlet fission harvest.

## 1. Introduction

Organic materials that undergo singlet fission can be used to strongly enhance the power conversion efficiency of single junction crystalline silicon (c-Si) solar cells<sup>1-2</sup>. To do so, a thin film of singlet fission-capable organic molecules with an optical gap approximately twice that of c-Si is implemented on the front surface of a c-Si solar cell. Photons absorbed within this layer trigger singlet fission, an exciton multiplication process that produces two triplet excitons from one optically-excited singlet state<sup>3-4</sup>. If these

triplet excitons are converted to photocurrent in the device, a significant portion of the solar energy that is usually lost to charge carrier thermalization in c-Si is instead turned into additional photocurrent, increasing the limiting efficiency of the cell from 32% to 45%<sup>1</sup>. This approach is akin to using a tandem structure that absorbs high-energy photons in a second absorber material with a larger fundamental gap. However, the tandem device produces photocurrent at two different junctions. Current matching imposes a cell design challenge and significantly reduces the cell efficiency under non-optimal conditions<sup>2</sup>. The singlet fission approach, having no need for current matching, completely avoids this limitation.

Tetracene (Tc) is a small organic molecule that efficiently undergoes singlet fission and has a triplet exciton energy ( $E_{T1}$ ) that is slightly larger than the band gap of c-Si ( $E_{Si}$ ). These two materials are thus thought to make an ideal pair for a singlet-fission enhanced solar cell. Exploiting singlet fission in these devices requires harvesting the triplet excitons at the Tc/c-Si interface. It appears evident from several attempts<sup>5-8</sup> that the interface needs to be modified to realize an efficient triplet harvest.

Most notably, triplet harvesting could be unambiguously shown for Tc on n-type Si covered with an ultrathin ( $\approx 1$  nm)  $\text{HfO}_x\text{N}_y$  layer<sup>9</sup>. Interestingly, no indication of triplet transfer was observed when using p-type Si<sup>10</sup>. The authors argue that this difference is due to the more favorable energy-level alignment (ELA) in the case of n-type Si, which gives rise to a lower charge-transfer (CT) state energy than for p-type Si.

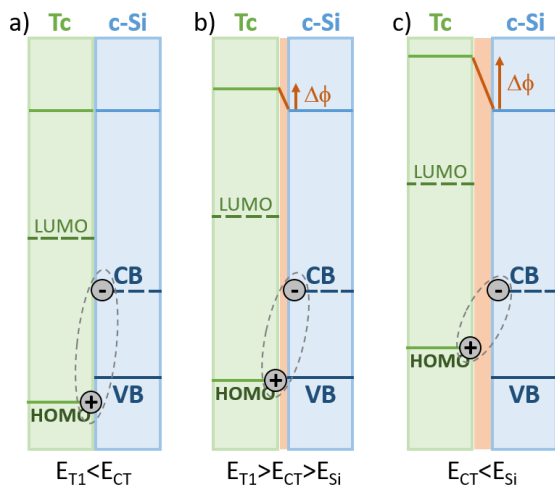


*Figure 1: Energy-level diagrams of Tc/c-Si interfaces for three different configurations between the energies of the Tc triplet state ( $E_{T1}$ ), the charge transfer state ( $E_{CT}$ ), and the Si band gap ( $E_{Si}$ ). The modified interface and the induced interface dipole ( $\Delta\phi$ ) are indicated in orange. Note that the shown combination of one-particle energy levels and two-particle excited state energies is only valid in cases where correlation effects between the electron-hole pair are negligible. This condition is not fulfilled for the Tc triplet exciton and we refrain from including it here.*

A proven strategy for changing the CT state energy is to implement a dipole layer at the interface<sup>11</sup>. This approach is the focus of the current work and is illustrated in Figure 1, which shows three characteristic situations that can arise after interfacial electron transfer from the tetracene triplet into an interface charge transfer exciton. Fig. 1 a) assumes that the unmodified ELA has a CT state with energy ( $E_{CT}$ ) higher than the  $T_1$  state ( $E_{T1}$ ). In this situation, the formation of the CT state is associated with an energy cost. Fig. 1 b) depicts a modified interface with a more favorable ELA for triplet energy transfer. In this case, both the formation of the CT state and the subsequent creation of an electron-hole pair in silicon are exothermic. Finally, Fig. 1 c) shows a more pronounced adjustment of the ELA where the energy of the CT state is lower

than the band gap of silicon. This configuration might be suitable in cases where a dissociation of the triplet excitons across a heterojunction at the interface is targeted.

Dipole layers can be implemented via polar molecules<sup>11</sup>. We used an alternative approach, wherein interlayers induce a preferential electron redistribution in the direction perpendicular to the interface. This scheme has been employed previously, e.g., to significantly enhance the exciton transfer yield at the ZnO-organic interface<sup>12</sup>.

We used two different classes of adsorbates to increase the work function of hydrogen-passivated Si (H-Si): i) organic electron-acceptor molecules, which induce electron transfer from the substrate and should leave the hydrogen passivation intact, and ii)  $\text{NF}_3$  gas or plasma, which react with the H-Si surface and exchange the hydrogen passivation with more electronegative species (F and  $\text{NF}_2$ ). We show that both approaches allow tuning of the ELA. Furthermore, for scheme i) we resolved concomitant changes in Tc morphology and built solar cells that contain the modified interfaces. The device results, which suggested no appreciable Tc triplet harvesting despite successful tuning of the ELA, point to limitations in the strategy of ELA modification, and suggest that this is at best a partial solution to the problem of triplet exciton harvesting in hybrid singlet fission solar cells.

## 2. Methods

### Si surface modification and characterization

The (100)- or (111)-oriented, n-type c-Si substrates were first cleaned with the RCA method and dipped in buffer HF or buffer  $\text{NH}_4\text{F}$  immediately before they were introduced in the vacuum system.

The c-Si wafer  $\text{NF}_3$  treatment was conducted in an RF driven capacitively-coupled plasma enhanced chemical vapor deposition (PECVD) chamber located at the Energy Materials In-Situ Laboratory Berlin (EMIL)<sup>13</sup> jointly operated by Helmholtz-Zentrum Berlin für Materialien und Energie, GmbH (HZB) and the Max-Planck Society (MPG). The base pressure of the chamber was  $<10^{-6}$  mbar. The electrode sizes were 6 inches and the lower electrode was mobile in order to confine the plasma within the desired volume. Additionally, a remote plasma source (RPS) equipped with an individual power source was attached on top of this chamber where the dissociation of the precursor gas takes place; the formed radicals flow through the shower head to the deposition chamber. The PECVD chamber was also utilized as a conventional CVD chamber. The process parameters according to deposition schemes are listed in Table 1 below. An optical emission spectrum of the plasma during the PECVD is included in the Supporting Information as Figure S1, allowing identification of the presence of  $\text{N}_2$ ,  $\text{N}_2^+$ , and  $\text{NF}$ , but not F in this case.

Table 1. Process conditions for the employed  $\text{NF}_3$  deposition techniques.

Process parameters	CVD	PECVD	RPS
Substrate Temperature ( $^{\circ}\text{C}$ )	360	180	180
Deposition Pressure (mbar)	2.4	1	1
Electrode Spacing (mils)	2240	700	700
$\text{NF}_3$ Flow Rate (sccm)	20	50	50
Applied RF Power (W)	-	100	800
Deposition Time (s)	600/3600	15	180

Tc (99.99 %) and  $\text{C}_{60}$  (99.9 %) were purchased from Sigma Aldrich and 2,2'-(perfluoronaphthalene-2,6-diylidene)dimalononitrile (F6TCNNQ) was provided by the Marder group (Georgia Tech). See Figs. 2 and 3 for chemical structures. Molecular films were deposited from resistively heated crucibles. The rates were determined with a quartz crystal microbalance. Rates of  $\approx 0.015 \text{ \AA/s}$  were used for  $\text{C}_{60}$  and F6TCNNQ. A

Tc deposition rate of 0.17 Å/s was employed at the LowDosePES endstation (see below) while the rate was 1 Å/s in all other cases.

Ultraviolet and X-ray photoelectron spectroscopy (UPS/XPS) measurements for the F6TCNNQ interlayer and NF<sub>3</sub> studies were performed at EMIL, using an Omicron Argus CU hemispherical energy analyzer. He I (21.22 eV) and Al K<sub>α</sub> (1486.7 eV) radiation from non-monochromatized sources were used for sample excitation. UPS measurements for the Tc thickness series on pristine and C<sub>60</sub>-covered H-Si(111) were performed at the LowDosePES endstation<sup>14</sup>, located at the PM 4 beamline of BESSY II (HZB). These spectra were collected with a Scienta SES 100 hemispherical energy analyzer and an excitation energy of 35 eV. The secondary electron cut-off (SECO) regions were measured with a bias of either -8.95 V or -10 V to clear the spectrometer work function. When comparing UPS spectra measured at EMIL and PM 4, the different experimental conditions give rise to differences in spectral shape. In particular:

- Photoemission intensity depends on the energies of the incoming photon and outgoing photoelectron. Both are different in the two cases for a given binding energy value.
- The two photoelectron analyzers have different acceptance angles and thus integrate different parts of the photoelectron momentum space.
- Secondary electrons in a given binding energy range are more important in the case of lower excitation energy.
- Electrons that contribute to the SECO feature have small kinetic energies and are thus very sensitive to the details of the applied electrostatic field between sample and photoelectron analyzer.

For two-photon photoemission spectroscopy (2PPE), a 150 kHz optical pulse train was generated with a regeneratively-amplified Ti:sapphire laser system driving two low-power non-collinear optical parametric amplifiers (NOPAs), which provided tuneable pulses in the visible range. Subsequent second-harmonic generation of the output of one NOPA provided UV photons for the probe pulse. The time delay between pump and probe pulses was produced using an electronically controlled delay stage to vary the optical path of the pump beam. The probe beam photon energy was maintained at  $h\nu_{\text{probe}} = 4.6$  eV, and the pump photon energy was set at  $h\nu_{\text{pump}} = 2.5$  eV. High time resolution in the 2PPE experiments was obtained by compressing the pulses with prism pairs, and the pump-probe in a cross correlation was 65 fs FWHM. The kinetic energy of the photoemitted electrons was measured with a homemade time-of-flight spectrometer. A -1 V bias voltage applied between the sample and the opening of the spectrometer to improve signal levels was compensated for during calculation of the electron kinetic energies. The 2PPE sample was grown by depositing 60 nm Tc on H-Si(111) in a separate UHV chamber. The sample was then transported to the 2PPE system under N<sub>2</sub>, where it was measured at 210 K.

Atomic-force microscopy (AFM) for investigating the effect of the C<sub>60</sub> interlayer was performed with a Park Systems XE-70. For the F6TCNNQ study, a MultiMode Atomic Force Microscope was used. AFM topographies were analyzed with the open source software Gwyddion.

X-Ray diffraction (XRD) measurements were carried out in the X-Ray CoreLab at HZB on a Bruker D8 X-Ray diffractometer equipped with a LynxEye detector and using Cu K- $\alpha_{1+2}$  radiation in either in Bragg-Brentano or Grazing-Incidence geometry. All diffraction data have been analyzed using the Diffraction software and the ICDD PDF4+ database.

Silicon photoluminescence (PL) transients were excited with a pulsed dye laser (MNL103 from LTB) having a pulse width of 3 ns, a pulse energy of 70 μJ, and a wavelength of 765 nm. The silicon related PL signal was directed through a 1130 nm interference filter and into a Si avalanche diode (EMM). Transients were collected and averaged using a digital oscilloscope (Agilent 5000 series).

## **Device fabrication and characterization**

Device fabrication began with a 4-inch diameter 280  $\mu\text{m}$  thick, (111)-oriented,  $3 \Omega \text{ cm}^{-1}$  resistivity, phosphorus-doped float zone-grown c-Si wafer, polished on both sides and cleaned with the RCA method. The design of the electron-selective contact is based on the high efficiency silicon heterojunction concept, and was fabricated as described in Ref <sup>15</sup>, omitting the conventional indium-doped tin oxide layer to reduce the device complexity. The resulting structure consists of the c-Si wafer, a 4 nm intrinsic hydrogenated amorphous Si (a-Si:H) layer and a 15 nm highly-doped n-type a-Si:H layer. After fabrication of the rear contact by thermal evaporation of 750 nm of silver, the substrate was cut into a series of  $1 \text{ cm}^2$  half-cells.

Each half-cell was then immersed in dilute hydrofluoric acid (1%, 2 min). After removal of the acid in a nitrogen gas stream, the substrates were immediately placed in a nitrogen-filled glovebox, then loaded into a thermal evaporator housed within it. Layers of F6TCNNQ,  $\text{C}_{60}$ , and Tc were grown by thermal evaporation at a base pressure of  $10^{-6}$  mbar. The deposition rates were  $0.5 - 1 \text{ \AA/s}$  for Tc,  $0.1 - 0.3 \text{ \AA/s}$  for  $\text{C}_{60}$ , and  $0.1 \text{ \AA/s}$  for F6TCNNQ, as determined by a quartz crystal microbalance. After deposition of the molecular films, samples were moved back into the nitrogen glovebox, and a commercial pre-mixed dispersion of PEDOT:PSS (Clevios F HC solar, Heraeus) was spin-coated (HZB: 1500 rpm, 10 s; AMOLF: 5000 rpm, 30 s) over the Tc layer. Samples were then annealed for 90 min in a vacuum oven at 330 K. This resulted in a PEDOT:PSS layer thickness of  $60 - 100 \text{ nm}$ , determined using scanning electron microscopy measurements of cleaved samples. For the metallization of the front contact, a silver contact grid was evaporated through a shadow mask.

At HZB, J-V-characteristics were measured by first adjusting a solar simulator in output power such that the short circuit current of a calibrated reference solar cell was equal to the value at AM1.5g. Devices were attached with their silver back contact to a copper plate using conductive epoxy and measurements were carried out in a four-probe setup using a Keithley source-measure unit. The copper plates with devices on top were fixed pneumatically on a metal chuck, for contacting the back of the cell. The silver front grid was contacted with two gold wires, in order to extract the holes. The metal chuck was kept at a constant temperature of  $25 \text{ }^\circ\text{C}$ . At AMOLF, J-V measurements were made in a two-probe configuration using an Agilent B2902A source-measure unit without temperature stabilization, using an Oriel Sol2A Xenon lamp with a 1-sun intensity as illumination.

External quantum efficiency (EQE) spectra measured at HZB were acquired using a home-built setup utilizing a 300 W xenon lamp, a monochromator (CS260, Newport), a lock-in amplifier, and mechanical chopping of the incident beam. A calibrated silicon solar cell was used to establish reference values. Measurements at AMOLF utilized a commercially-produced system (Newport QuantX 300). All EQE measurements were carried out in air.

### 3. Results and discussion

#### **Tc/H-Si(111) reference**

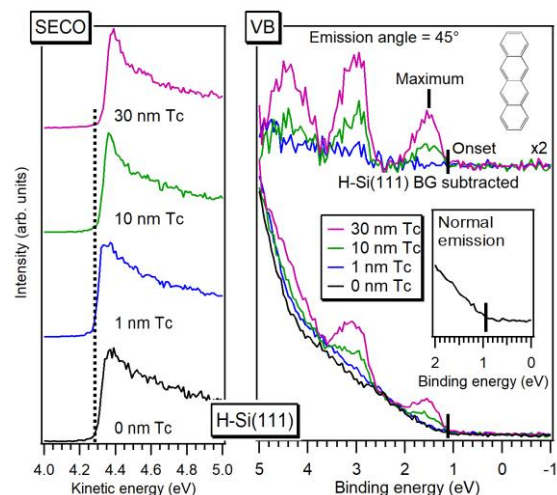


*Figure 2: SECO and VB spectra for H-Si(111) before and after the depositions of Tc films of the indicated thicknesses. The energetic positions that are used to determine the work function and electronic energy-levels are indicated by a dashed line and solid ticks, respectively. All VB spectra were measured with the sample tilted by 45° with respect to the electron analyzer in order to enhance the surface sensitivity. The exception is the Si VB onset that is shown in the inset and was measured in normal emission geometry. The top part reports the chemical structure of Tc and magnified VB spectra for which the H-Si(111) signal has been subtracted to enhance the Tc-derived spectral intensity.*

We began by investigating the unmodified Tc/H-Si(111) interface. Figure 2 shows the secondary electron cut-off (SECO) and valence band (VB) regions for a Tc thickness series on H-Si(111). The SECO allows to derive the sample's work function and is unchanged throughout the whole series, as indicated by the vertical dashed line. Thus, there is no significant work function change upon interface formation, meaning that the vacuum levels of c-Si and Tc align. There is only little Tc-derived spectral intensity visible for 1 nm Tc coverage, which clearly demonstrates that Tc exhibits Volmer-Weber growth on H-Si(111) when grown at room temperature<sup>16</sup>. The deduced ELA will be discussed in detail later on. Here we only note that theoretical calculations predict the Tc highest occupied molecular orbital (HOMO) to be lower in energy than the Si VB<sup>17</sup>, i.e. a configuration inverse to what we observed from UPS. A part of this discrepancy might be due to the fact that the calculations were performed for the intimate interface and include the full screening of the Si surface while the experiments probed mostly Tc in thicker films (due to the Volmer-Weber growth mode) where the screening should be less efficient. Another relevant contribution possibly stems from the fact that the Tc orientation that was considered in Ref. <sup>17</sup> is more upright than the one that has recently been derived for ultrathin Tc on H-Si<sup>16</sup>. Due to electrostatic effects, ionization energies for Tc films with the molecules in an inclined configuration should be higher than for those with more upright molecules<sup>18</sup>, as has been observed for related molecules<sup>19-20</sup>.

### **Increasing the H-Si work function**

The employed strategy for tuning the ELA is based on the assumption that the modification induces a preferential electronic rearrangement at the c-Si surface and that no significant further interface dipole is induced upon deposition of the Tc layer (ideally: vacuum-level alignment). Accordingly, the potential step that adjusts the Tc/c-Si ELA is supposed to manifest itself as a corresponding increase of the H-Si work function (cf. Fig. 1).

*Acceptor molecules on H-Si(111)*

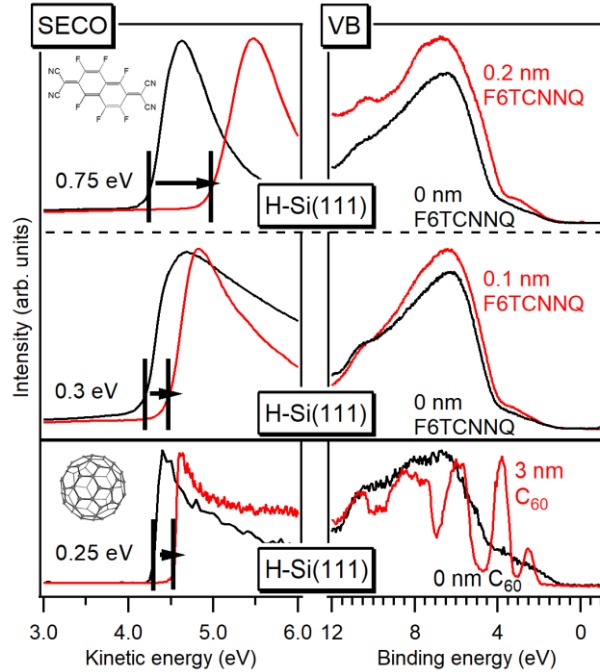


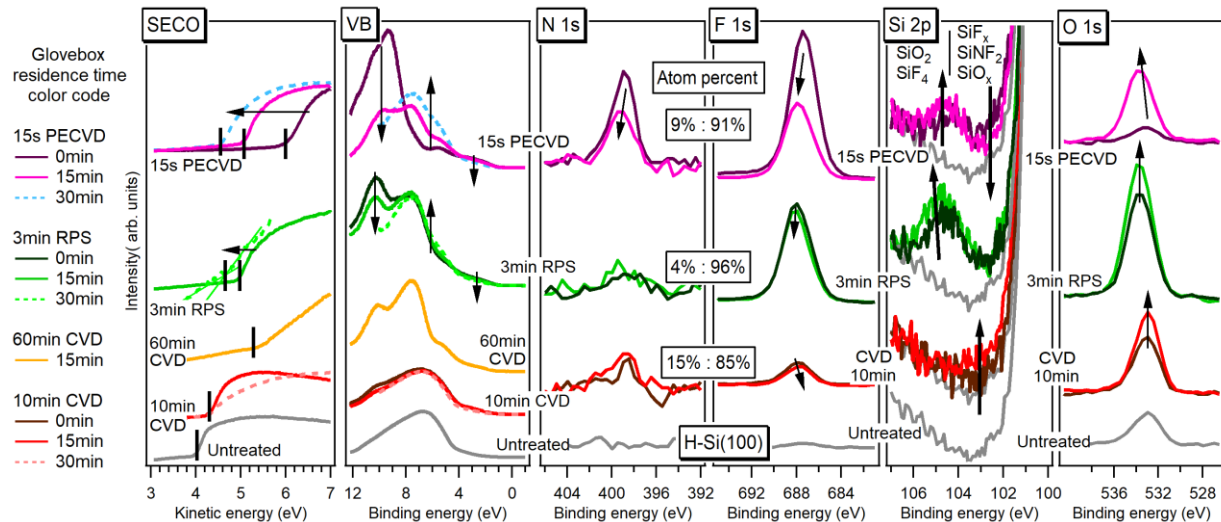
Figure 3: SECO and VB regions for H-Si(111) before and after the depositions of F6TCNNQ (top) and C<sub>60</sub> (bottom) films of the indicated coverages. All spectra were measured in normal emission geometry. The origins of the different spectral shapes in the F6TCNNQ and C<sub>60</sub> series are discussed in the methods section, The chemical structures of F6TCNNQ and C<sub>60</sub> are included in the upper and lower left corner, respectively.

Figure 3 shows the UPS spectral changes induced when depositing 3 nm C<sub>60</sub>, 0.1 nm F6TCNNQ, or 0.2 nm F6TCNNQ on H-Si(111). In all three cases, the formation of the molecular layer gives rise to an increased work function, as derived from the SECO. The valence band spectrum for 3 nm C<sub>60</sub> (corresponding to three monolayers) is dominated by C<sub>60</sub>-derived features, which is evidence for a closed film. By contrast, the F6TCNNQ coverages correspond to the submonolayer regime. Accordingly, the Si valence band spectral shape is apparent in the spectra, but efficient surface wetting is evident by clear spectral changes compared to H-Si(111). Despite the larger coverage, the C<sub>60</sub> film gives the smallest work-function increase out of the three samples. This is due to the fact that C<sub>60</sub> is only a relatively weak acceptor. The electron affinity of C<sub>60</sub> is 4.0 eV<sup>21</sup>, which is significantly lower than that of F6TCNNQ at 5.6 eV<sup>22</sup>. We note that the H-Si(111) work function has been reported to increase by more than 1.7 eV to almost 6 eV when F6TCNNQ coverages > 1 nm were used<sup>23</sup>.

#### NF<sub>3</sub> treatment of H-Si(100)

Functionalizing the c-Si surface with a species of high electronegativity is an alternative means of controlling the c-Si work function. Changing the termination of H-Si(100) to halogen atoms has been investigated theoretically<sup>24</sup> and the work function of F-Si(100) is calculated to be 6.1 eV, which is > 0.6 eV higher than for other halogens. Similar values were also predicted for Si(111)<sup>25</sup>.

In this work, we employed NF<sub>3</sub> in order to change the H-termination of H-Si(100). We distinguish three different cases: (i) H-Si(100) that was directly exposed to an NF<sub>3</sub> plasma (a PECVD process); (ii) H-Si(100) that was exposed to NF<sub>3</sub> plasma generated in a remote plasma source (RPS); and (iii) H-Si(100) that was heated to 360 °C and exposed to neutral NF<sub>3</sub> (a CVD process). Important differences are expected between these cases. While NF<sub>3</sub> plasma is very efficient in etching c-Si, neutral NF<sub>3</sub> has been reported to not etch c-Si surfaces notably<sup>26-27</sup>.



*Figure 4: UPS and XPS results for three different  $\text{NF}_3$  treatments. The Glovebox residence time after  $\text{NF}_3$  treatment is indicated via the color and line-style code shown on the left hand side. Corresponding spectral changes are indicated by arrows. Differences in SECO shape are mainly due to differences in the type of sample holder used. SECO spectra are absent in cases where the employed sample holder was not equipped for applying a bias voltage. No XPS was performed for the '60 min CVD' sample.  $\text{SiF}_4$  is a gas and a corresponding signal would stem from physisorbed etching products. All spectra were measured in normal emission geometry. See the main text for more details.*

Figure 4 presents the UPS and XPS results which show the work function development as well as changes in the valence band and chemical surface structure. The 15s PECVD sample shows the most pronounced trends of the samples examined in this work. Most importantly, the work function directly after the PECVD treatment (dark violet curves) is 6.0 eV, as can be seen in Fig. 4. This is very close to the predicted value of 6.1 eV for F-Si(100)<sup>24</sup>. It is also much larger than reported work functions for Si surfaces terminated with other electronegative groups<sup>24, 28-30</sup> and slightly higher than the value observed for F6TCNNQ<sup>23</sup>. For this sample, we observe a valence band with a characteristic peak at 10 eV. A similar spectral shape was observed after fluorination of carbon nanotubes<sup>31</sup> and we can attribute the main peak to F 2p-like states<sup>31-32</sup>. Unlike what was observed in the case of carbon nanotube fluorination<sup>31</sup>, we find that the PECVD treatment increases the density of states close to the Fermi level. In Fig. 4 we can see a pronounced F 1s signal with a very similar binding energy to the small F 1s signal for the  $\text{NH}_4\text{F}$ -cleaned H-Si(100) reference (shown in gray). All these data are consistent with successful c-Si surface fluorination, which is also in line with theoretical work suggesting that  $\text{NF}_3$  adsorption leads to the formation of silicon atoms terminated with F<sup>33-34</sup>. These theoretical studies also propose that part of the Si atoms become terminated with  $\text{NF}_2$ . The N 1s spectrum in Fig. 4 shows that N is indeed present after PECVD, albeit with a much lower abundance than expected from the stoichiometry of  $\text{NF}_3$ . The atomic fractions of N and F are stated in Fig. 4, showing that the N fraction of all samples was significantly less than the 25% expected if all  $\text{NF}_3$  atoms remained on the surface. An F 1s spectrum measured with lower pass energy (not shown) yields that the peak maximum is located at 687.2 eV, as expected for a mixture of F-Si and F bound to a more electronegative element like N<sup>35-36</sup>. We note that our data agree with a previous study that showed that chemisorption of  $\text{NF}_3$  onto Si(100) results in the formation of Si-F and Si-N bonds with sub-stoichiometric N<sup>26</sup>. The escape of nitrogen atoms is possible in the form of  $\text{NF}_x$  and  $\text{N}_2$  gas.

The chemical shifts of the Si 2p core level binding energy induced by changing Si-Si bonds to Si-F bonds<sup>37-40</sup> are very similar to those observed when Si-Si bonds change to Si-O bonds<sup>41</sup>, making it impossible to deduce the chemical species from the Si 2p spectra alone. We therefore use the F 1s and O 1s spectra to

assist the assessment. We find that for the as-deposited PECVD sample, the atom percentage of F is 20 times that of O. This allows attributing the majority of the PECVD-induced Si 2p spectral intensity to Si-F<sub>x</sub> bonds.

Next, we look at the changes induced by exposure of our F- and NF<sub>2</sub>-terminated Si sample to a glovebox (Working gas: N<sub>2</sub>, O: 0.1 – 1 ppm, H<sub>2</sub>O: < 0.1 ppm) environment. In the corresponding spectra (pink curves) we can clearly see significantly decreased N 1s and F 1s signals while the O 1s signal has increased and is now located at higher binding energy, at a value that is expected for oxidized Si<sup>42</sup>. In view of these trends we can link the decreased (increased) spectral intensity below (above) approximately 104 eV in the Si 2p spectrum to a removal of Si-F and Si-NF<sub>2</sub> species (formation of SiO<sub>2</sub>) and the shift of the F1s to the formation of Si-O-F<sup>43</sup>. The pronounced oxidation under glove box conditions that is observed for the PECVD-treated sample is likely due to the rough surface of this sample, which is created when the NF<sub>3</sub> plasma etches the c-Si surface. Indeed, AFM micrographs included in Figures S6 and S7 of the Supporting Information clearly show the strong etching effect of the PECVD treatment.

The corresponding valence band spectrum is now less dominated by the F-derived features. The new spectral intensity can be explained by contributions from SiO<sub>x</sub>, and SiN<sub>x</sub><sup>44-45</sup>. The dashed blue spectrum was obtained after another exposure to the N<sub>2</sub> atmosphere and exhibits a continuation of the same trend. As can be seen in the SECO region, the gradual replacement of Si-F and Si-NF<sub>2</sub> with SiO<sub>2</sub> results in a large and continued decrease of the work function.

For the RPS-treated H-Si(100) we also find evidence of a fluorine-rich surface. This time the nitrogen fraction is even smaller, but the O content is now more than 50 % of that of F already for the freshly RPS-treated sample. The RPS-induced Si 2p spectral intensity thus likely stems from fluorinated and oxidized Si atoms. Possibly, a part of the surface exhibits Si-O-F groups as has been proposed for NF<sub>3</sub> exposure in the presence of residual oxygen<sup>33, 36</sup>.

We can use the O 1s and F 1s intensity trends observed when going from the fresh to the N<sub>2</sub>-aged PECVD and RPS samples to deduce the origin of the valence band features. This corroborates our assessment that the peak at 10 eV and the states below 4 eV stem from F-derived states, while the features in between originate predominately from O-derived states. Very similar work functions are observed for the RPS and PECVD samples after the same short aging in the glovebox (5.0 eV and 5.1 eV, respectively).

We now turn our attention to the CVD procedure. In contrast to PECVD and RPS, no NF<sub>3</sub> plasma is generated. Instead, the H-Si(100) surface is exposed to neutral NF<sub>3</sub> gas. A much less aggressive attack of the surface is expected in this case<sup>26-27</sup>. For a 10 minute exposure, all effects are much less pronounced than for both PECVD and RPS. However, also in this case the valence band and core level spectra show similar indications for the creation of a partly F- and NF<sub>2</sub>-terminated Si(100) surface. Consistently, we find that the work function slightly increased to 4.3 eV. Even after aging in N<sub>2</sub> we observe no SiO<sub>2</sub>, but indication for sub-oxide formation. A longer CVD treatment of 60 minutes gives rise to a much higher work function (~5.3 eV). This value and the valence band features are similar to those observed for RPS and PECVD, indicating that eventually similar effects occur in all cases. However, we did not investigate prolonged CVD in detail.

## **Energy-level alignment tuning**

*T<sub>c</sub> on the C<sub>60</sub> interlayer*

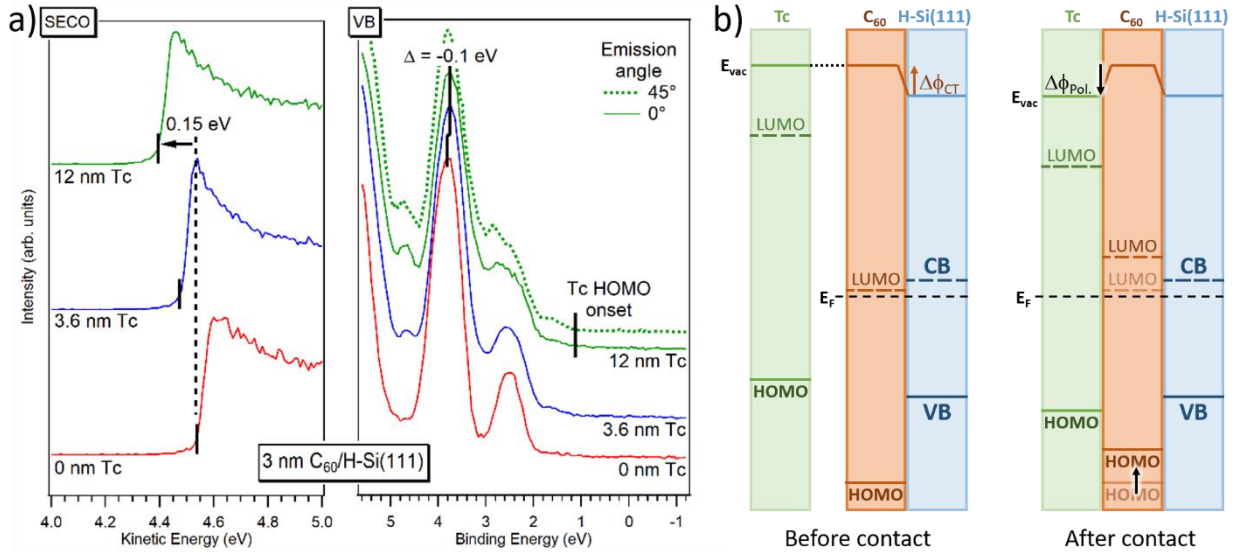


Figure 5: a) UPS results for 3 nm  $C_{60}/H-Si(111)$  before and after Tc deposition of the indicated coverages. All spectra were measured in normal emission geometry, except the dotted spectrum for 12 nm Tc for which the sample was tilted by  $45^\circ$ . The increased surface sensitivity for this measurement geometry enhances the spectral weight of the surface layer and allows to more accurately determine the Tc HOMO onset. Right: Schematic energy-level diagrams that illustrate the shift of the energy-levels upon Tc making contact with  $C_{60}/H-Si(111)$ . See main text for details.

We have seen in Fig. 3 that  $C_{60}$  deposition increases the H-Si(111) work function by 0.25 eV. We will now look in detail at the electronic changes induced by the formation of the Tc overlayer. From the valence band spectra reported in Figure 5 a) it becomes clear that although new spectral intensity emerges upon Tc deposition, the Tc-derived features do not dominate the spectral shape even for a 12 nm Tc coverage which corresponds to approximately 10 monolayers. This clearly shows that the Volmer-Weber growth mode of Tc that was observed for H-Si(111) also prevails for  $C_{60}$ -covered H-Si(111). As can be seen from the corresponding SECOs, the deposition of Tc gives rise to a gradual decrease of the work function. At a coverage of 12 nm, the decrease amounts to 0.15 eV. Given the pronounced Volmer-Weber growth it is conceivable that there are still open patches in the Tc film and the saturation work function after complete Tc/ $C_{60}$  interface formation is slightly lower. This means that the total work function increase induced by the  $C_{60}$  interlayer amounts to  $< 0.1$  eV. Accordingly, we expect at most a small shift of the Tc HOMO towards the Fermi level. Indeed, the Tc HOMO onset, determined from Fig. 5, is located at 1.1 eV, i.e. the same value as for H-Si(111).

Given that Tc has the same ELA with respect to both pristine and  $C_{60}$ -modified H-Si(111), it is tempting to attribute this result to Tc's intrinsic work function. However, the numbers of Tc's intrinsic charge carriers as well as charge carriers injected from the substrate into Tc are too low to saturate the band bending at the Tc/substrate interface within Tc film thicknesses of a few 10 nm<sup>46</sup>. Therefore such thin Tc films do not exhibit an intrinsic work function and their ELA with respect to the substrate is not fixed. The ELA flexibility is limited by the Fermi-level pinning of the HOMO and LUMO, which is discussed below in the context of F6TCNNQ interlayers.

No Fermi-level pinning is expected under the ELA conditions that we observe for Tc on  $C_{60}/H-Si(111)$ . Therefore, the potential drop that gives rise to the work function decrease upon formation of the Tc/ $C_{60}$  interface has to derive from a specific interaction between Tc and  $C_{60}/H-Si(111)$ . Two scenarios are conceivable: An interaction between Tc and  $C_{60}$  and an interaction between Tc and H-Si(111). To decide

between the two, we determine concomitant shifts in the  $C_{60}$  and Tc energy levels and visualize them in Fig. 5 b). For  $C_{60}$ , we can see a prominent peak in Fig. 5 a) that is located at 3.8 eV before Tc deposition. Upon Tc deposition, this peak shifts by 0.1 eV towards lower binding energies. For Tc, the ELA before contact can be derived by asserting vacuum-level alignment at the  $C_{60}$ /Tc interface and using Tc's ionization energy. We employ the Tc film on H-Si(111) discussed above (*cf.* Fig. 2) and calculate the ionization energy by taking the sum of the work function (4.25 eV) and the HOMO onset with respect to the Fermi level (1.1 eV). The difference between the determined ionization energy of Tc (5.35 eV) and the work function of  $C_{60}$ /H-Si(111) (4.55 eV) then gives the energetic position of the Tc HOMO onset with respect to the Fermi level of  $C_{60}$ /H-Si(111) before contact (0.8 eV). With respect to this situation, the Tc HOMO onset after contact is shifted by 0.3 eV to higher binding energies. As illustrated in Fig. 5 b), this means that the  $C_{60}$  energy-level shift upon contact formation is opposite to that of Tc. This behavior is a clear evidence for the formation of an interface dipole directly at the Tc/ $C_{60}$  interface. In contrast, for an assumed c-Si substrate-to-Tc overlayer charge transfer (across the  $C_{60}$  interlayer), the energy levels of both Tc and  $C_{60}$  would shift in the same direction<sup>47-48</sup>.

Two different effects could be at the origin of the interface dipole at the Tc/ $C_{60}$  interface. First, a similar interface dipole was observed previously at the related pentacene/ $C_{60}$  interface<sup>49</sup> and ascribed to a polarization of the molecules' electronic clouds<sup>50-51</sup>. Second, Tc and  $C_{60}$  form a donor-acceptor heterojunction for which the generation of photovoltage has been observed<sup>52-54</sup>.

As can be seen from the 'after contact' energy-level diagram in Fig. 5 b), the combined effect of the interface dipoles at the Tc/ $C_{60}$  and the  $C_{60}$ /H-Si(111) interfaces results in an unchanged effective ELA between Tc and c-Si.

#### Tc on F6TCNNQ interlayers and $NF_3$ -treated c-Si

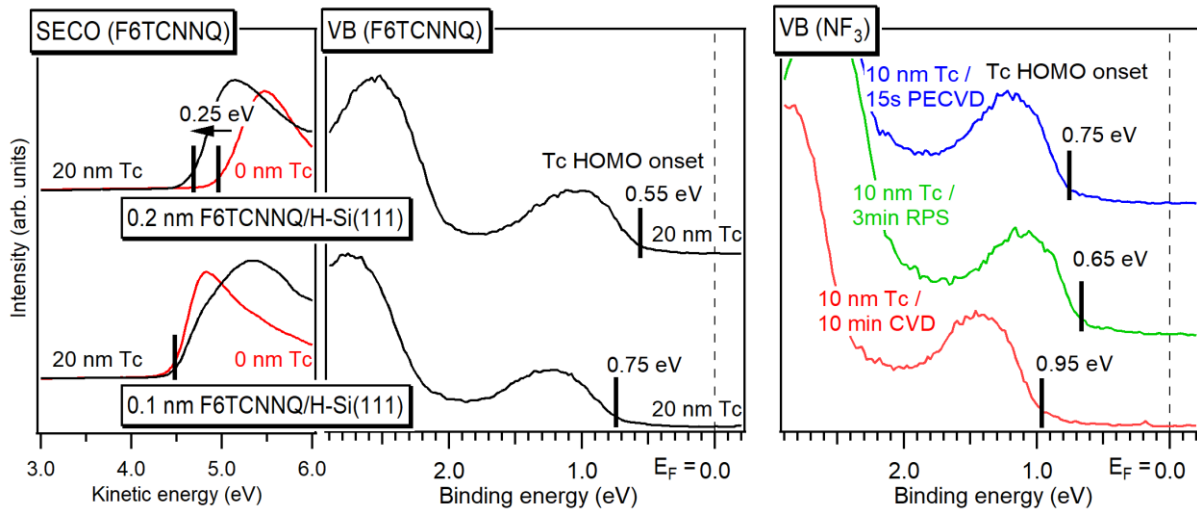


Figure 6: Left: SECO region for F6TCNNQ-modified H-Si(111) before and after deposition of 20 nm Tc. Middle and right: Tc HOMO region for 20 nm Tc on F6TCNNQ-modified H-Si(111) (emission angle = 30°) and 10 nm Tc on  $NF_3$ -modified H-Si(100) (normal emission), respectively. For the  $NF_3$ -modified c-Si samples, the Tc deposition took place immediately after the 30 min exposure to glovebox conditions reported as dashed lines in Fig. 4.

Figure 6 presents valence band spectra for Tc films on F6TCNNQ- and  $NF_3$ -modified c-Si. The Tc thickness was 20 nm (10 nm) in the case of F6TCNNQ ( $NF_3$ ). We see that all F6TCNNQ and  $NF_3$  depositions give rise to smaller energy differences between the Tc HOMO and the Fermi level than observed for pristine H-

Si(111) (*cf.* Fig. 2). This proves that both modification schemes can be used to tune the ELA. The smallest Tc HOMO onset binding energy observed in this work is 0.55 eV for 0.2 nm F6TCNNQ. However, this is still less than expected from the observed work function increase at the F6TCNNQ/H-Si(111) interface for the same system. This discrepancy is due to a work function decrease upon formation of the Tc/F6TCNNQ interface that is apparent from the SECO shift shown in Fig. 6. This observation resembles the behavior discussed above for Tc/C<sub>60</sub> and we cannot exclude a similar origin in both cases. However, in the case of the thinner F6TCNNQ interlayer the formation of the Tc overlayer does not induce a notable work function change, indicating that another mechanism is at play. The more likely explanation then is Fermi level pinning of the Tc HOMO. This phenomenon occurs once the tailing gap states of the Tc HOMO start overlapping with the Fermi level and prevents further reduction of the energy distance between the two.<sup>55-57</sup>

## Morphology

### Acceptor molecule interlayers

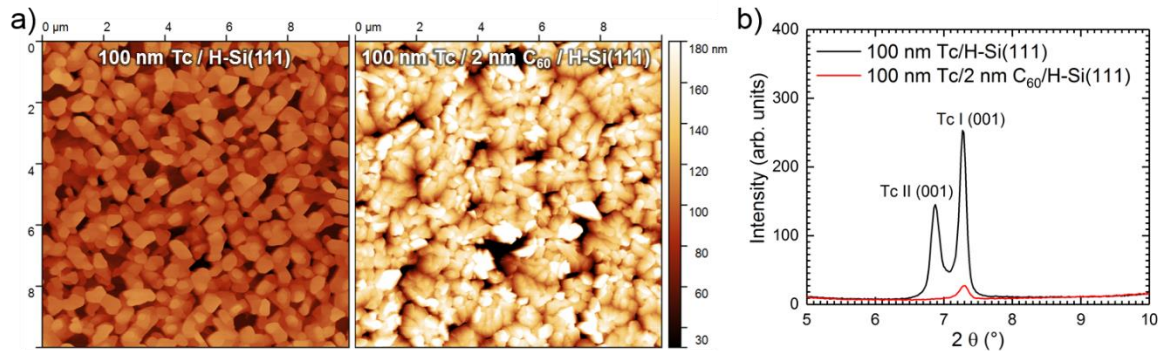


Figure 7: a) AFM images for the indicated systems. b) XRD data for the same films as in a).

Figure 7 a) presents AFM images for Tc on H-Si(111) and on 2 nm C<sub>60</sub>/H-Si(111). In both cases, the Tc thickness is 100 nm. For Tc on H-Si(111), large column-like grains are observed. The Tc film on the C<sub>60</sub> interlayer is much rougher and the grains are smaller and have significantly less orientational order. Fig. 7 b) shows X-ray diffractograms obtained for the two systems. The two diffraction peaks found for Tc directly on H-Si(111) are well known as corresponding to the so-called thin film (Tc II) and bulk-like (Tc I) phases, whose relative abundances strongly depend on Tc deposition conditions<sup>58-59</sup>. For the Tc films grown on top of the C<sub>60</sub> interlayer, only a small Tc I signal and no Tc II signal is observed.

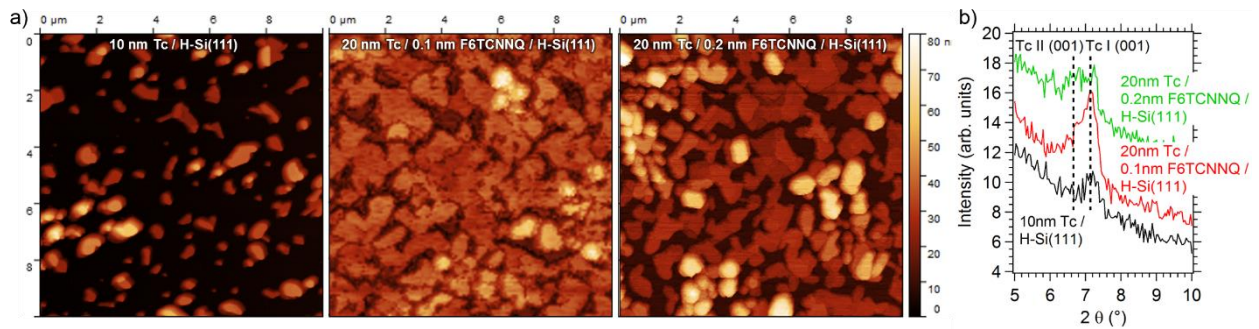


Figure 8: a) AFM images for the indicated systems. b) XRD data for the same films as in a). The red and green curves have been vertically offset by 2 and 4, respectively, for clarity.

Figure 8 a) shows AFM images for 10 nm Tc on H-Si(111) as well as for 20 nm Tc both on 0.1 nm and 0.2 nm F6TCNNQ interlayers on H-Si(111). The morphology is rather similar in all three cases. Note that the Tc film thicknesses are nominal values. Since these samples stayed hours to days in the UHV system after Tc deposition, considerable dewetting likely occurred. Indeed, the Tc thicknesses derived from AFM is less than 8 nm for the nominally 10 nm film on H-Si(111). The relatively low film thickness for all three samples is one reason why the corresponding diffractograms presented in Fig. 8 b) exhibit much smaller Tc diffraction peaks than were observed for the 100 nm films discussed above. In addition, their breadth is much larger due to the smaller average crystallite size. Lastly, the slope of the background indicates a possible amorphous contribution to the film. Still, the data suggest that the 0.1 nm F6TCNNQ interlayer distorts the Tc crystallinity only a little compared to the H-Si(111) reference while the 0.2 nm F6TCNNQ has a somewhat larger effect. Indications for the Tc II phase is observed for both F6TCNNQ interlayer thicknesses. These results suggest that the sub-monolayer F6TCNNQ interlayers affect the Tc morphology less than the super-monolayer C<sub>60</sub> interlayer. This is consistent with the qualitatively similar AFM-derived morphologies in the case of F6TCNNQ [Fig. 8 a)] and drastic differences observed for C<sub>60</sub> [Fig. 7 a)].

## Photovoltaic performance

### Acceptor molecule interlayers

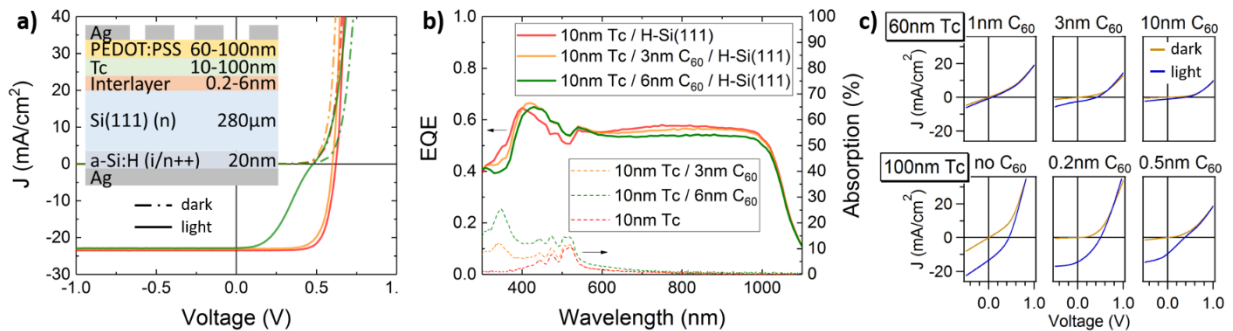


Figure 9 a) and b): J-V curves for the indicated systems and corresponding EQE and absorption spectra, respectively (HZB). The schematic device architecture is also shown. c) top (bottom): Devices with C<sub>60</sub> interlayers of at least (less than) one monolayer and a Tc layer thickness of 60 nm (100 nm) (AMOLF).

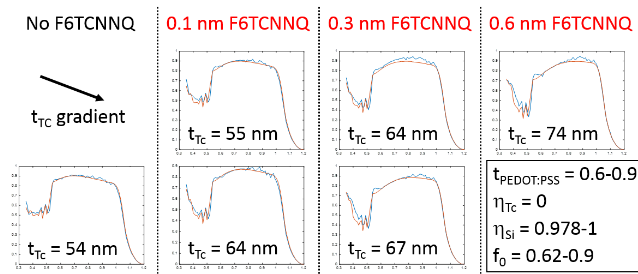
In a previous work, a Tc layer was implemented within the layer stack of a silicon heterojunction solar cell without distorting the performance of the cell<sup>6</sup>. We used the identical architecture and implemented the molecular interlayers as an extra deposition step before laying down the Tc film. The cell structure is included as an inset in Figure 9 a).

Fig. 9 presents device characteristics for cells with C<sub>60</sub> interlayers. Panel a) shows the J-V-curves for devices with 10 nm Tc and C<sub>60</sub> interlayers of 0 nm (red), 3 nm (orange), and 6 nm (green) thickness. The curves for the C<sub>60</sub>-free cell and for a device with an interlayer of 3 nm C<sub>60</sub> are virtually identical. Both devices have a short circuit current density of approximately 23 mA/cm<sup>2</sup>, an open circuit voltage of about 610 mV, and a fill factor slightly above 70%. Overall, this results in solar conversion efficiencies of  $\eta \approx 10\%$ . The device containing 6 nm C<sub>60</sub> on the other hand exhibits a low open circuit voltage of about 480 mV and a strongly reduced fill factor of about 40%, reducing the efficiency to about 4.5%. The s-shape can be explained by unfavorable energy levels in C<sub>60</sub> for hole injection and a low mobility of the Tc layer.<sup>60-61</sup> Further support for the notion that C<sub>60</sub> interlayers give rise to a decreased Tc mobility is provided below.

Fig. 9 b) present the EQE for the same devices and the absorption spectra for the molecular films (Tc and C<sub>60</sub>). Comparing the two allows to identify that one dip in the EQE at 350 nm and multiple dips at 440 nm,

475 nm, 505 nm, and 520 nm correspond to  $C_{60}$  and Tc absorption, respectively. This shows that both layers give rise to parasitic absorption. In the region where Tc absorbs, no qualitative change of the EQE shape induced by the  $C_{60}$  interlayer can be seen that would point to efficient triplet exciton harvest (peaks instead of dips). This is consistent with our UPS experiments that found that the effective ELA is the same with and without  $C_{60}$  interlayer. A small increase in the Tc EQE can be seen when normalizing the spectra to the  $C_{60}$ -free reference (*cf.* Supplementary Figure S2), but this change is most likely due to optical effects induced by the  $C_{60}$  interlayer via changes in Tc and PEDOT:PSS morphology and possibly an additional contribution from exciton dissociation at the Tc/ $C_{60}$  interface<sup>52-54</sup>.

We also produced a matrix of devices with Tc thicknesses of 10 nm, 30 nm, 60 nm and 100 nm and  $C_{60}$  thicknesses of 0 nm, 1 nm, 3 nm and 10 nm. The J-V curves are shown in Fig. 9 c). Note that the cells were fabricated under less ideal conditions and thus exhibit higher series and lower shunt resistances than those discussed above. Cells containing  $\geq 1$  nm  $C_{60}$  lose their performance completely already at 60 nm Tc thicknesses, while those with  $< 1$  nm  $C_{60}$  work up to 100 nm Tc. If we recall that we found from XRD and AFM that Tc deposited onto a  $C_{60}$  interlayer exhibited low crystallinity and high roughness, it seems reasonable to attribute the increased Tc-thickness sensitivity for cells with a full  $C_{60}$  monolayer to a Tc morphology that is less favorable for efficient hole transport than the films found for Tc deposited directly on H-Si(111).



*Figure 10. EQE spectra for solar cells with different F6TCNNQ interlayer and Tc thicknesses (AMOLF) and corresponding fits according to optical modelling. The internal quantum efficiency for Tc was set to zero. The Tc thickness ( $t_{TC}$ ) derived from the fit is shown for each spectrum. Fit parameter ranges are given for the PEDOT:PSS thickness ( $t_{PEDOT:PSS}$ ), the internal quantum efficiency for Si ( $\eta_{Si}$ ), and the fraction of the birefringent PEDOT:PSS overlayer presenting the ordinary optical axis to the surface normal. The  $t_{TC}$  trend induced by differences in molecular flux during device fabrication is indicated by the arrow.*

Figure 10 presents selected EQE spectra for cells that contain F6TCNNQ interlayers of 0, 0.1, 0.3, or 0.6 nm. The corresponding J-V-curves and additional EQE spectra are shown as Supporting Figures S3 and S4, respectively. We modelled the EQE curves by simulating the optical and electric response of the layer stack<sup>6</sup>. Optical simulation was by the transfer matrix method, using the GenPro4 package.<sup>62</sup> All EQE spectra can be described well when setting the internal quantum efficiency of the Tc layer to zero. Spectral differences are fully accounted for by differences in Tc layer thickness. Differences in Tc thickness are indeed expected for this device series, because the sample holder could not be rotated during the deposition run. The fact that the Tc growth mode sensitively depends on the deposition rate<sup>63</sup> can enhance these differences further. Our results thus do not indicate a significant change of the Tc triplet harvest efficiency for F6TCNNQ-modified interfaces.

### *NF<sub>3</sub> treatment*

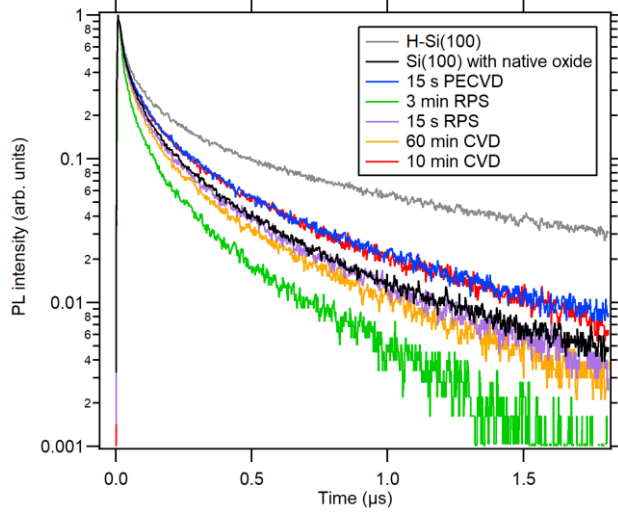


Figure 11: Time-resolved normalized PL transients for the indicated samples.

We anticipate that due to the aggressive nature of the  $\text{NF}_3$  treatment, the most important aspect for the modified c-Si surfaces is whether their passivation is still sufficient for efficient photovoltage generation in c-Si. We have therefore investigated the passivation by measuring the decay of the c-Si-related PL signal. Figure 11 shows the transients for a number of different treatments.

Si(100) with native oxide and hydrogen termination are shown as black and gray lines, respectively. These samples serve as references with interface state densities that are typically on the order of  $10^{12} \text{ eV}^{-1}\text{cm}^{-2}$ <sup>64-65</sup> and  $10^{11} \text{ eV}^{-1}\text{cm}^{-2}$ <sup>66</sup>, respectively. All  $\text{NF}_3$ -treated surfaces show worse surface passivation than H-Si(100), but treatments with CVD for 10 minutes or PECVD for 15 s yield slightly better passivation than that of a native oxide layer. Prolonged CVD or RPS treatments result in continued deterioration of the surface passivation.

Note that – except for ‘60 min CVD’ – the samples used for the PL experiments are not identical to the ones used for the photoelectron spectroscopy measurements shown in Fig. 4. The UPS data for the PL samples are shown in Supplementary Figure S5.

## 4. Discussion

A successful interface modification scheme has to improve at least one problematic aspect of the unmodified interface. To identify whether the Tc/c-Si ELA is a problem for singlet fission harvesting, we first have to relate the ELA with the triplet dynamics that we want to steer. This is not at all trivial, because a triplet exciton is an electronic excitation that, in its simplest representation, is described as two bound particles (electron and hole) interacting with their environment. Experiments that probe excitons usually measure energy differences (e.g., optical transitions) that do not directly correspond to energy-level differences of the two non-interacting single particles. In contrast, the energy levels depicted in one-particle energy-level diagrams are ionization energies and electron affinities, which correspond to final states with one extra hole or electron, respectively, and can be reported on an absolute single-particle scale, e.g., with the vacuum level or the Fermi level as reference point.

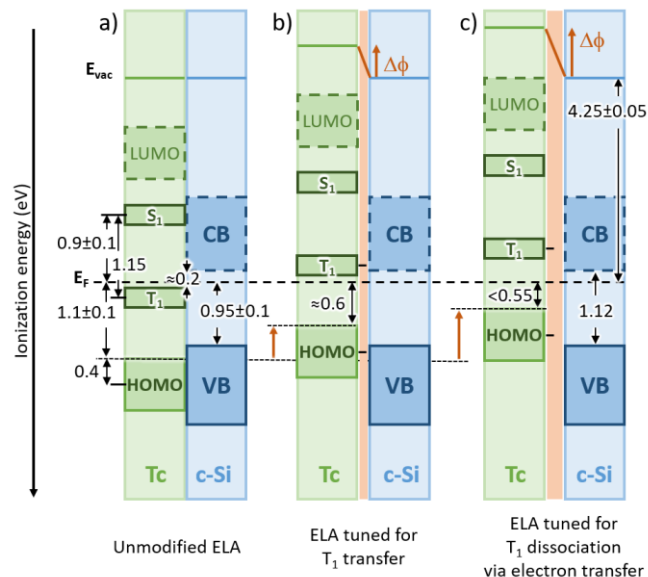


Figure 12: Schematic one-particle energy-level diagram. a): Energy levels for the unmodified Tc/H-Si(111) interface. The energy levels for the Tc HOMO and H-Si(111) VB were derived from the data shown in Fig. 2. The position of the peak maximum of the Tc  $T_1$  state was deduced from two-photon photoemission data presented in Ref.<sup>67</sup>. Unoccupied states do not have an ionization energy and the Tc LUMO is indicated only for completeness. b) and c): Energy-level diagrams with shifted Tc/c-Si ELA due to the introduction of interface dipoles of two different magnitudes. See text for details.

As discussed in Ref.<sup>68</sup>, one has to be particularly careful when discussing excited states of organic molecules in a one-particle energy-level diagram, as, for example, the difference between the HOMO ionization energy and the lowest unoccupied molecular orbital (LUMO) electron affinity (the transport gap) deviates significantly from exciton energies due to electron correlation effects. One consistent approach is to use the ionization energies of the Tc HOMO and the Tc triplet state ( $T_1$ )<sup>68</sup>, as shown in Figure 12. For Tc, we include the LUMO only for completeness. In contrast, for c-Si we assume correlation effects to be negligible and the CB electron affinity to be identical to its ionization energy.

Further confusion arises from the fact that not always the same peak feature is deemed relevant in photoemission experiments when extracting the ionization energies and electron affinities. While it is generally assumed that the *onset* (or leading edge) of emission approximately coincides with the mobility edge of the corresponding orbital or band and is thus most relevant for charge transport at interfaces<sup>69</sup> (but tailing gap states have to be considered<sup>70</sup>), exciton energies are often reported as distances between the peak *maxima*<sup>67</sup>.

Consequently, we combine these considerations in order to draw a consistent and complete picture, as compiled in the energy-level diagram shown in Fig. 12 a). This diagram is based on our UPS results for Tc/H-Si(111) and 2PPE results for Tc previously reported by Tritsch *et al.*<sup>67</sup>. We consider both peak maximum and onset. The difference between Tc HOMO ( $T_1$ ) maximum and onset is 0.4 – 0.5 eV (0.15 – 0.2 eV<sup>67</sup>). According to the derived diagram, electron transfer from Tc  $T_1$  to Si CB represents an energy cost  $\geq 0.2$  eV in the absence of ELA tuning.

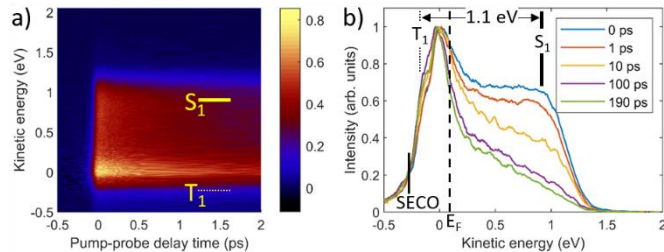


Figure 13. a) Two-dimensional plot of background-subtracted 2PPE data for 60 nm Tc/H-Si(111). b) One-dimensional slices of the data in a) at the indicated times. The  $S_1$  and  $T_1$  positions were determined by visual inspection and comparison with the time series measured for another Tc film reported previously<sup>67</sup>. The Fermi level position that is indicated in b) was determined from the known probe beam energy and photoelectron analyzer work function.

This analysis is further supported by additional 2PPE measurements performed on 60 nm Tc/H-Si(111). The 2PPE data were first cleared of the constant background by subtracting a spectrum measured at negative time delays. The resulting spectra, shown in Figure 13, clearly show a short-lived feature with its maximum slightly below 1 eV kinetic energy. Its shape and temporal evolution agrees favorably with the Tc  $S_1$  feature found in Ref. <sup>67</sup>. As can be seen in Fig. 13 b), this feature lies  $0.85 \pm 0.1$  eV above the Fermi level, i.e., just where one would expect the Tc  $S_1$  state to be located based on the analysis shown in Fig. 12. The situation at lower kinetic energies is more complex. A long-lived feature can be seen around 0 eV. However, the energy difference with respect to the  $S_1$  peak is too low for this peak to derive from the Tc  $T_1$  state and we tentatively attribute it to unoccupied gap states from defects or surface contaminants as well as photoemission from occupied states that is not completely removed by our background subtraction procedure. A much weaker feature can be seen at approximately 0.25 eV below the Fermi level, i.e. at a distance from  $S_1$  that matches well the energy difference between Tc  $T_1$  and Tc  $S_1$ <sup>9,67</sup>.

We next discuss how more favorable ELA configurations can be achieved. To drive energy transfer (and suppress single charge carrier back-transfer), it is preferable to achieve a symmetric alignment, where the Tc  $T_1$  maximum is just above the c-Si CB and the Tc HOMO maximum is just below the c-Si VB onset. As illustrated in Fig. 12 b), this can be achieved by shifting the Tc energy levels by  $\approx 0.5 \pm 0.2$  eV towards lower binding energies.

To promote exciton dissociation, we instead want the Tc HOMO maximum to be located above the VB onset. For this, the required shift of the Tc levels towards lower binding energies is  $> 0.55$  eV, as depicted in panel c). Notably, such an alignment is beyond what was experimentally found in our UPS measurements (*cf.* Fig. 6), likely due to Fermi-level pinning of the Tc HOMO. However, we note that in such cases of Fermi-level pinning, a closer proximity between HOMO and Fermi level is typically found at the immediate interface<sup>56</sup>, which was not probed in these experiments. In addition, much closer proximity between the HOMO onset and Fermi level was reported for tetraseleno-tetracene<sup>20</sup>, suggesting suitable Tc functionalization as a possible strategy should more pronounced adjustments become necessary.

Another aspect to take into account is the c-Si band bending induced by formation of the contact layer. It has been shown that the band bending contribution to the total potential difference at the interface can be modified via the bulk dopant concentration and, for moderate doping levels more importantly, via the surface state density.<sup>71</sup> Induced band bending was reported for PEDOT:PSS/H-Si<sup>72</sup>, and chemically functionalized c-Si<sup>73</sup>. In contrast, for the F6TCNNQ/H-Si(111) interfaces investigated in this work we did not discern any notable effect within the experimental resolution of 0.1 eV, in agreement with other studies<sup>23</sup>.

Intriguingly, for Tc on  $\text{HfO}_x\text{N}_y$ -modified c-Si, the reported Tc HOMO (Si CB) onset is at 1.4 (-0.35) eV binding energy (i.e. referenced to the Fermi level)<sup>9</sup>. For this ELA, Tc  $T_1$  to c-Si CB electron transfer should be even less favorable (by 0.5 eV) than for pristine H-Si(111). In great contrast to this expectation, the  $T_1$  energy transfer yield with the  $\text{HfO}_x\text{N}_y$  interlayer was reportedly significantly boosted. This could mean that energy-level diagrams such as the one in Fig. 12 do not capture all relevant energy contributions for exciton transfer processes.

In a second attempt to arrive at a meaningful energy-level diagram, we use the one-particle energy levels together with two-particle energy levels (*cf.* Fig. 1). As pointed out above, this is only valid if the electron and hole that make up the excited state are not strongly bound. For the CT state, the hole is located on the organic molecule while the electron is in c-Si. Calculations predict only a low binding energy for such hybrid inorganic-organic CT states due to the more pronounced screening and delocalization induced by c-Si;<sup>74-75</sup>. The CT state energy should then approximately correspond to the HOMO-CB difference and such a correspondence has indeed been reported<sup>11</sup>. If we apply this approach and calculate the CT state energy as the energy difference of the onsets of Tc HOMO and c-Si CB, we obtain CT state energies of 1.25 eV, identical to the Tc  $T_1$  energy. This calculation thus predicts an isoenergetic  $T_1$ -to-CT state transfer, whereas the analysis based on the ionization energies discussed above yields an energy barrier of 0.2 eV. This difference derives from the fact that the former relies on using the Tc HOMO onset, while the latter uses the Tc HOMO maximum. The 0.2 eV difference is simply the peak-width difference between Tc HOMO and Tc  $T_1$  (*cf.* Fig. 12). For the  $\text{HfO}_x\text{N}_y$ -modified interface, the CT state-based analysis yields a CT state energy of 1.75 eV, reiterating that the  $\text{HfO}_x\text{N}_y$  interlayer should not enhance the interface performance, but deteriorate it.

This apparent discrepancy might derive from a relevant energy contribution that we did not consider in our arithmetic, possibly due to an inconsistent derivation of the relevant energy levels (onset vs. maximum, Gaussian vs. exponential tail), a lack of experimental sensitivity (due to the Vollmer-Weber growth mode we mostly probe Tc that is not directly at the interface and most employed methods average over the heterogeneous surface area), or unaccounted final-state effects and excited-state processes. Unfortunately, different spectral features had to be compared in Ref. <sup>11</sup> and whether a finite energy offset between the absolute values of CT state energy and HOMO-CB difference exists remains an open question. A hidden offset that rigidly shifts the ELAs could rationalize the results for the F6TCNNQ-containing devices, which nominally exhibit a trend to more favorable ELA/CT state energy but whose EQE data indicate no improvement of the exciton yield. We note in passing that, consistently, a preliminary analysis of PL transients measured for Tc films on F6TCNNQ-modified H-Si(111) (not shown) does not indicate a significant acceleration of the delayed fluorescence decay that would indicate an enhanced Tc  $T_1$  quenching compared to pristine H-Si(111).

On the other hand, aspects not related to the ELA could be at the origin of the increased triplet-harvest yield of  $\text{HfO}_x\text{N}_y$ -modified interfaces and the absence of a notable EQE enhancement for the F6TCNNQ-containing solar cells.  $\text{HfO}_x\text{N}_y$  interlayers might assist forward triplet energy transfer by inducing suitable interface states<sup>76</sup> or transient electrostatic fields<sup>77</sup>, or suppress backward transfer by increasing the electrostatic screening and the electron-hole pair separation in the charge transfer state<sup>77-78</sup>. Possible non-ELA-related effects of the modifications presented in this work are considered in the following section.

### **Secondary effects of the interface modification**

Having discussed the interface energetics above, we now deal with secondary effects induced by the interface modification and how they might affect the kinetics of relevant processes.

First of all, the changes in the Tc morphology and polymorphism we observed by XRD and AFM will affect crucial aspects of the excited state dynamics like exciton transport<sup>79-80</sup> and the singlet fission rate<sup>58, 81</sup>. In

addition, the orientation at the interface is critical. Forward interfacial charge transfer is favored by orbital overlap, which is larger for face-on Tc<sup>82</sup> and smaller if a molecular interlayer acts as spacer. On the other hand, an increased spatial separation of electron-hole pairs in the CT state induced by acceptor-molecule interlayers should reduce back transfer and interface recombination in cases where transport into the c-Si bulk is limited by kinetics<sup>78</sup>. Pentacene stands upright on C<sub>60</sub><sup>83-84</sup> and we propose that Tc on C<sub>60</sub> will likely adopt the same orientation. At this point we have no information about the adsorption geometries of Tc on F6TCNNQ or NF<sub>3</sub>. We note that CVD of NF<sub>3</sub> was found to sometimes result in the absence of Tc molecules after thermal deposition, which we interpret as a Teflon-like effect induced by the F-termination.

Furthermore, the interfacial charge transfer yield depends on the density of states (DOS) of the charge acceptor<sup>78</sup>. Thus, changes of the c-Si surface electronic structure induced by the interface modifier might affect the transfer processes. Clear changes of the c-Si surface DOS induced by prolonged or aggressive NF<sub>3</sub> treatment are apparent from the valence band spectra. In contrast, C<sub>60</sub> deposition does not disturb the H-termination of H-Si(111)<sup>85</sup>. Fluorinated molecules can etch non-terminated Si(111)<sup>86</sup>, but we have no indication from our data or the literature that fluorinated molecules attack the H-termination. For F6TCNNQ and the related F4TCNQ on H-Si(111), theoretical calculations that assume intact hydrogen passivation yield electronic structures that are consistent with corresponding experimental results<sup>23, 87</sup>.

## 5. Conclusions

The presented device characteristics and PL transients show that the implementation of the presented interface modification schemes is compatible with well-performing solar cells. However, detrimental effects on the cell performance have been observed when exceeding certain layer coverages and NF<sub>3</sub> treatment limits. Positive and negative effects have to be carefully balanced.

We could show that both the insertion of the strong acceptor molecule F6TCNNQ as well as the exchange of the c-Si H-termination with F and NF<sub>2</sub> can be used to shift the ELA by up to approximately 0.5 eV. In contrast, no notable effective change was induced when using the weaker acceptor molecule C<sub>60</sub> as interlayer. The ELA modifications can reverse the Tc HOMO to c-Si VB alignment: For pristine H-Si(111), the Tc HOMO is lower in energy than the c-Si VB. In contrast, the modified interface forms a type II heterojunction with the Tc HOMO well above the c-Si VB. In the case of F6TCNNQ, the magnitude of the shift can be tuned via the coverage. For c-Si fluorination, the NF<sub>3</sub> nature (neutral gas, remote or direct plasma) as well as the duration of the treatment can be utilized to the same effect. This fine-tuning allows realizing a type I heterojunction. We propose that even larger shifts are prevented by Fermi-level pinning of the Tc HOMO and would require chemical functionalization of Tc.

In view of these results, it is disappointing that we can find no clear signs for an enhancement of the Tc exciton harvest in the EQE behavior of the Tc/c-Si devices. This either shows that the considered energy levels are not a limiting factor for exciton energy transfer, or that changing the ELA is not a sufficient condition for an efficient Tc exciton harvest. While beyond the scope of our manuscript, we deem the answer to this possible discrepancy highly relevant for a rational improvement of Tc/c-Si interfaces specifically and organic-inorganic interfaces in general.

ELA tuning via molecular acceptor and donor interlayers is compatible with many different kinds of surfaces<sup>88-89</sup>. Therefore, it can be readily combined with other interface modifiers like HfO<sub>x</sub>N<sub>y</sub>. This means that the presented results will be helpful for improving the triplet exciton harvest beyond the specific interfaces discussed in the current work. ELA tuning via NF<sub>3</sub> treatment of c-Si, on the other hand, offers new routes for controlling electronic interface properties in integrated circuits and other Si-based technologies.

## Associated Content

### Supporting Information

The Supporting Information is available free of charge on the ACS Publications website.

NF<sub>3</sub> optical emission spectrum during PECVD, normalized EQE spectra for solar cells with C<sub>60</sub> interlayers, device characteristics for solar cells with F6TCNNQ interlayers, UPS data for PL samples, and AFM micrograph of NF<sub>3</sub>-treated H-Si(100) (PDF)

### Acknowledgements

This work has been partially supported by the German Federal Ministry of Education and Research (BMBF) through the collaborative project EPRoC (contract number 01186916/1) and SISSY (contract number 03SF0403) as well as by the Helmholtz association (HGF) through the Helmholtz Energy Materials Foundry (HEMF) and within the framework of the HySPRINT Innovation lab.

The work of M.H.F., B.D. and B.E. is supported by the Dutch Research Council (NWO). RWM acknowledges the Helmholtz Association, Germany, for funding within the Helmholtz Excellence Network SOLARMATH, a strategic collaboration of the DFG Excellence Cluster MATH+ and Helmholtz-Zentrum Berlin (Grant ExNet-0042-Phase-2-3). M.B. acknowledges funding from the Helmholtz Association through the Excellence network UniSysCat (Grant ExNet-0029-Phase1).

We thank Yadong Zhang and Seth Marder (Georgia Tech) for providing the F6TCNNQ, Kerstin Jacob (HZB) for wafer cleaning, Carola Klimm (HZB) for SEM measurements, and Hazem Aldahhak and Uwe Gerstmann (U Paderborn) for stimulating discussions. JN thanks Thorsten Schultz, Ruslan Ovsyannikov, Johannes Frisch, Wolfgang Bremsteller (HZB), and Michael Hävecker (FHI) for support during the UPS experiments.

### References

1. Rao, A.; Friend, R. H. Harnessing singlet exciton fission to break the Shockley-Queisser limit. *Nat. Rev. Mater.* **2017**, *2* (11), 17063.
2. Futscher, M.; Rao, A.; Ehrler, B. The potential of singlet fission photon multipliers as an alternative to silicon-based tandem solar cells. *ACS Energy Lett.* **2018**, *3* (10), 2587-2592.
3. Smith, M. B.; Michl, J. Recent advances in singlet fission. *Annual Review of Physical Chemistry* **2013**, *64* (1), 361-386.
4. Smith, M. B.; Michl, J. Singlet fission. *Chem. Rev.* **2010**, *110* (11), 6891-6936.
5. Piland, G. B.; Burdett, J. J.; Hung, T.-Y.; Chen, P.-H.; Lin, C.-F.; Chiu, T.-L.; Lee, J.-H.; Bardeen, C. J. Dynamics of molecular excitons near a semiconductor surface studied by fluorescence quenching of polycrystalline tetracene on silicon. *Chem. Phys. Lett.* **2014**, *601*, 33 - 38.
6. MacQueen, R. W.; Liebhaber, M.; Niederhausen, J.; Mews, M.; Gersmann, C.; Jäckle, S.; Jäger, K.; Tayebjee, M. J. Y.; Schmidt, T. W.; Rech, B.; et al. Crystalline silicon solar cells with tetracene interlayers: the path to silicon-singlet fission heterojunction devices. *Mater. Horiz.* **2018**, *5*, 1065-1075.
7. Daiber, B.; Pujari, S. P.; Verboom, S.; Luxembourg, S. L.; Tabernig, S. W.; Futscher, M. H.; Lee, J.; Zuilhof, H.; Ehrler, B. A method to detect triplet exciton transfer from singlet fission materials into silicon solar cells: Comparing different surface treatments. *J. Chem. Phys.* **2020**, *152* (11), 114201.
8. Daiber, B.; Maiti, S.; Ferro, S. M.; Bodin, J.; van den Boom, A. F. J.; Luxembourg, S. L.; Kinge, S.; Pujari, S. P.; Zuilhof, H.; Siebbeles, L. D. A.; et al. Change in tetracene polymorphism facilitates triplet transfer in singlet fission-sensitized silicon solar cells. *J. Phys. Chem. Lett.* **2020**, *11* (20), 8703-8709.
9. Einzinger, M.; Wu, T.; Kompalla, J. F.; Smith, H. L.; Perkinson, C. F.; Nienhaus, L.; Wieghold, S.; Congreve, D. N.; Kahn, A.; Bawendi, M. G.; et al. Sensitization of silicon by singlet exciton fission in tetracene. *Nature* **2019**, *571* (7763), 90-94.

10. Baldo, M. A.; Wu, T.; Einzinger, M. Interlayers and associated systems, devices, and methods. U.S. Patent 20190372038 A1, 2019.
11. Piersimoni, F.; Schlesinger, R.; Benduhn, J.; Spoltore, D.; Reiter, S.; Lange, I.; Koch, N.; Vandewal, K.; Neher, D. Charge transfer absorption and emission at ZnO/organic interfaces. *J. Phys. Chem. Lett.* **2015**, *6* (3), 500-504.
12. Schlesinger, R.; Bianchi, F.; Blumstengel, S.; Christodoulou, C.; Ovsyannikov, R.; Kobin, B.; Moudgil, K.; Barlow, S.; Hecht, S.; Marder, S. R.; et al. Efficient light emission from inorganic and organic semiconductor hybrid structures by energy-level tuning. *Nat. Comm.* **2015**, *6* (1), 6754.
13. Lips, K.; Schulze, T. F.; Starr, D.E.; Bär, M.; Wilks, R.G.; Fenske, F.; Ruske, F.; Reiche, M.; van de Krol, R.; Reichardt, G.; et al. EMIL The energy materials in situ laboratory Berlin a novel characterization facility for photovoltaic and energy materials **2015**, <https://core.ac.uk/display/54062363>.
14. Giangrisostomi, E.; Ovsyannikov, R.; Sorgenfrei, F.; Zhang, T.; Lindblad, A.; Sassa, Y.; Cappel, U. B.; Leitner, T.; Mitzner, R.; Svensson, S.; et al. Low Dose Photoelectron Spectroscopy at BESSY II: Electronic structure of matter in its native state. *J. Electron. Spectrosc. Relat. Phenom.* **2018**, *224*, 68 - 78.
15. Mews, M.; Korte, L.; Rech, B. Oxygen vacancies in tungsten oxide and their influence on tungsten oxide/silicon heterojunction solar cells. *Solar Energy Materials and Solar Cells* **2016**, *158*, 77-83.
16. Niederhausen, J.; MacQueen, R. W.; Lips, K.; Aldahhak, H.; Schmidt, W. G.; Gerstmann, U. Tetracene ultrathin film growth on hydrogen-passivated silicon. *Langmuir* **2020**, *36* (31), 9099-9113.
17. Janke, S. M.; Rossi, M.; Levchenko, S. V.; Kokott, S.; Scheffler, M.; Blum, V. Pentacene and tetracene molecules and films on H/Si(111): Level alignment from hybrid density functional theory. *Electron. Struct.* **2020**.
18. Heimel, G.; Salzmann, I.; Duhm, S.; Koch, N. Design of organic semiconductors from molecular electrostatics. *Chem. Mater.* **2011**, *23* (3), 359-377.
19. Duhm, S.; Heimel, G.; Salzmann, I.; Glowatzki, H.; Johnson, R. L.; Vollmer, A.; Rabe, J. P.; Koch, N. Orientation-dependent ionization energies and interface dipoles in ordered molecular assemblies. *Nat. Mater.* **2008**, *7* (4), 326-332.
20. Niederhausen, J.; Duhm, S.; Heimel, G.; Bürker, C.; Xin, Q.; Wilke, A.; Vollmer, A.; Schreiber, F.; Kera, S.; Rabe, J. P.; et al. Seleno groups control the energy-level alignment between conjugated organic molecules and metals. *J. Chem. Phys.* **2014**, *140* (1), 014705.
21. Wilke, A.; Endres, J.; Hörmann, U.; Niederhausen, J.; Schlesinger, R.; Frisch, J.; Amsalem, P.; Wagner, J.; Gruber, M.; Opitz, A.; et al. Correlation between interface energetics and open circuit voltage in organic photovoltaic cells. *Appl. Phys. Lett.* **2012**, *101* (23).
22. Zhang, F.; Kahn, A. Investigation of the high electron affinity molecular dopant F6-TCNNQ for hole-transport materials. *Adv. Funct. Mater.* **2018**, *28* (1), 1703780.
23. Wang, H.; Levchenko, S. V.; Schultz, T.; Koch, N.; Scheffler, M.; Rossi, M. Modulation of the work function by the atomic structure of strong organic electron acceptors on H-Si(111). *Adv. Electron. Mater.* **2019**, *5* (5), 1800891.
24. Bertocchi, M.; Amato, M.; Marri, I.; Ossicini, S. Tuning the work function of Si(100) surface by halogen absorption: A DFT study. *Phys. Status Solidi c* **2017**, *14* (12), 1700193.
25. Arefi, H. H.; Fagas, G. Chemical trends in the work function of modified Si(111) surfaces: A DFT study. *J. Phys Chem. C* **2014**, *118* (26), 14346-14354.
26. Shorter, J. A.; Langan, J. G.; Steinfeld, J. I. Dissociative chemisorption of NF<sub>3</sub> at Si(100) surfaces. *Surf. Sci.* **1989**, *219* (3), L560-L564.
27. Ibbotson, D. E.; Mucha, J. A.; Flamm, D. L.; Cook, J. M. Plasmaless dry etching of silicon with fluorine-containing compounds. *J. Appl. Phys.* **1984**, *56* (10), 2939-2942.
28. Li, Y.; O'Leary, L. E.; Lewis, N. S.; Galli, G. Combined theoretical and experimental study of band-edge control of Si through surface functionalization. *J. Phys. Chem. C* **2013**, *117* (10), 5188-5194.
29. Lopinski, G. P.; Eves, B. J.; Hul'ko, O.; Mark, C.; Patitsas, S. N.; Boukherroub, R.; Ward, T. R. Enhanced conductance of chlorine-terminated Si(111) surfaces: Formation of a two-dimensional hole gas via chemical modification. *Phys. Rev. B* **2005**, *71* (12), 125308.

30. Hunger, R.; Jaegermann, W.; Merson, A.; Shapira, Y.; Pettenkofer, C.; Rappich, J. Electronic structure of methoxy-, bromo-, and nitrobenzene grafted onto Si(111). *J. Phys. Chem. B* **2006**, *110* (31), 15432-15441.
31. Bittencourt, C.; Van Lier, G.; Ke, X.; Suarez-Martinez, I.; Felten, A.; Ghijssen, J.; Van Tendeloo, G.; Ewels, C. P. Spectroscopy and defect identification for fluorinated carbon nanotubes. *ChemPhysChem* **2009**, *10* (6), 920-925.
32. Morikawa, E.; Choi, J.; Manohara, H. M.; Ishii, H.; Seki, K.; Okudaira, K. K.; Ueno, N. Photoemission study of direct photomicro machining in poly(vinylidene fluoride). *J. Appl. Phys.* **2000**, *87* (8), 4010-4016.
33. Endou, A.; Little, T. W.; Yamada, A.; Teraishi, K.; Kubo, M.; Ammal, S. S. C.; Miyamoto, A.; Kitajima, M.; Ohuchi, F. S. Chemical interaction of NF<sub>3</sub> with Si (Part II): Density functional calculation studies. *Surf. Sci.* **2000**, *445* (2), 243-248.
34. Miotto, R.; Ferraz, A. C.; Srivastava, G. P. Dissociative adsorption of NF<sub>3</sub> on Si(001)-(2×1). *Surf. Sci.* **2000**, *454-456*, 152-156.
35. Cao, X.; Hamers, R. J. Formation of a surface-mediated donor-acceptor complex: Co-adsorption of trimethylamine and boron trifluoride on the silicon (001) surface. *J. Phys. Chem. B* **2002**, *106* (8), 1840-1842.
36. Little, T. W.; Ohuchi, F. S. Chemical interaction of NF<sub>3</sub> ion beams and plasmas with Si (Part I): X-ray photoelectron spectroscopy studies. *Surf. Sci.* **2000**, *445* (2), 235-242.
37. Winters, H. F.; Coburn, J. W. Surface science aspects of etching reactions. *Surf. Sci. Rep.* **1992**, *14* (4), 162-269.
38. Morikawa, Y.; Kubota, K.; Ogawa, H.; Ichiki, T.; Tachibana, A.; Fujimura, S.; Horiike, Y. Reaction of the fluorine atom and molecule with the hydrogen-terminated Si(111) surface. *Journal of Vacuum Science & Technology A* **1998**, *16* (1), 345-355.
39. Nakamura, M.; Takahagi, T.; Ishitani, A. Fluorine termination of silicon surface by F<sub>2</sub> and succeeding reaction with water. *Jap. J. Appl. Phys.* **1993**, *32* (Part 1, No. 6B), 3125-3130.
40. McFeely, F. R.; Morar, J. F.; Shinn, N. D.; Landgren, G.; Himpsel, F. J. Synchrotron photoemission investigation of the initial stages of fluorine attack on Si surfaces: Relative abundance of fluorosilyl species. *Phys. Rev. B* **1984**, *30* (2), 764-770.
41. Himpsel, F. J.; McFeely, F. R.; Taleb-Ibrahimi, A.; Yarmoff, J. A.; Hollinger, G. Microscopic structure of the SiO<sub>2</sub>/Si interface. *Phys. Rev. B* **1988**, *38* (9), 6084-6096.
42. Jensen, D. S.; Kanyal, S. S.; Madaan, N.; Vail, M. A.; Dadson, A. E.; Engelhard, M. H.; Linford, M. R. Silicon (100)/SiO<sub>2</sub> by XPS. *Surf. Sci. Spectra* **2013**, *20* (1), 36-42.
43. Haring, R. A.; Liehr, M. Reactivity of a fluorine passivated silicon surface. *Journal of Vacuum Science & Technology A* **1992**, *10* (4), 802-805.
44. Gritsenko, V. A.; Shaposhnikov, A. V.; Kwok, W. M.; Wong, H.; Jidomirov, G. M. Valence band offset at silicon/silicon nitride and silicon nitride/silicon oxide interfaces. *Thin Solid Films* **2003**, *437* (1), 135-139.
45. Kobayashi, H.; Mizokuro, T.; Nakato, Y.; Yoneda, K.; Todokoro, Y. Nitridation of silicon oxide layers by nitrogen plasma generated by low energy electron impact. *Appl. Phys. Lett.* **1997**, *71* (14), 1978-1980.
46. Ishii, H.; Sugiyama, K.; Ito, E.; Seki, K. Energy level alignment and interfacial electronic structures at organic/metal and organic/organic interfaces. *Adv. Mater.* **1999**, *11* (8), 605-625.
47. Niederhausen, J.; Amsalem, P.; Wilke, A.; Schlesinger, R.; Winkler, S.; Vollmer, A.; Rabe, J. P.; Koch, N. Doping of C<sub>60</sub> (sub)monolayers by Fermi-level pinning induced electron transfer. *Phys. Rev. B* **2012**, *86*, 081411.
48. Amsalem, P.; Niederhausen, J.; Wilke, A.; Heimel, G.; Schlesinger, R.; Winkler, S.; Vollmer, A.; Rabe, J. P.; Koch, N. Role of charge transfer, dipole-dipole interactions, and electrostatics in Fermi-level pinning at a molecular heterojunction on a metal surface. *Phys. Rev. B* **2013**, *87*, 035440.
49. Kang, S. J.; Yi, Y.; Kim, C. Y.; Cho, S. W.; Noh, M.; Jeong, K.; Whang, C. N. Energy level diagrams of C<sub>60</sub>/pentacene/Au and pentacene/C<sub>60</sub>/Au. *Synth. Met.* **2006**, *156* (1), 32-37.

50. Verlaak, S.; Beljonne, D.; Cheyns, D.; Rolin, C.; Linares, M.; Castet, F.; Cornil, J.; Heremans, P. Electronic structure and geminate pair energetics at organic/organic interfaces: The case of pentacene/C<sub>60</sub> heterojunctions. *Adv. Funct. Mater.* **2009**, *19* (23), 3809-3814.
51. Linares, M.; Beljonne, D.; Cornil, J.; Lancaster, K.; Brédas, J.-L.; Verlaak, S.; Mityashin, A.; Heremans, P.; Fuchs, A.; Lennartz, C.; et al. On the interface dipole at the pentacene–fullerene heterojunction: A theoretical study. *J. Phys. Chem. C* **2010**, *114* (7), 3215-3224.
52. Chu, C.-W.; Shao, Y.; Shrotriya, V.; Yang, Y. Efficient photovoltaic energy conversion in tetracene-C<sub>60</sub> based heterojunctions. *Appl. Phys. Lett.* **2005**, *86* (24), 243506.
53. Wu, T. C.; Thompson, N. J.; Congreve, D. N.; Hontz, E.; Yost, S. R.; Voorhis, T. V.; Baldo, M. A. Singlet fission efficiency in tetracene-based organic solar cells. *Appl. Phys. Lett.* **2014**, *104* (19), 193901.
54. Jadhav, P. J.; Mohanty, A.; Sussman, J.; Lee, J.; Baldo, M. A. Singlet exciton fission in nanostructured organic solar cells. *Nano Lett.* **2011**, *11* (4), 1495-1498.
55. Niederhausen, J.; Amsalem, P.; Frisch, J.; Wilke, A.; Vollmer, A.; Rieger, R.; Müllen, K.; Rabe, J. P.; Koch, N. Tuning hole-injection barriers at organic/metal interfaces exploiting the orientation of a molecular acceptor interlayer. *Phys. Rev. B* **2011**, *84*, 165302.
56. Oehzelt, M.; Koch, N.; Heimel, G. Organic semiconductor density of states controls the energy level alignment at electrode interfaces. *Nat. Comm.* **2014**, *5*, 4174.
57. Koch, N. Electronic structure of interfaces with conjugated organic materials. *Phys. Status Solidi RRL* **2012**, *6* (7), 277-293.
58. Arias, D. H.; Ryerson, J. L.; Cook, J. D.; Damrauer, N. H.; Johnson, J. C. Polymorphism influences singlet fission rates in tetracene thin films. *Chem. Sci.* **2016**, *7*, 1185-1191.
59. Nahm, R. K.; Engstrom, J. R. Who's on first? Tracking in real time the growth of multiple crystalline phases of an organic semiconductor: Tetracene on SiO<sub>2</sub>. *J. Chem. Phys.* **2017**, *146* (5), 052815.
60. Wagner, J.; Gruber, M.; Hinderhofer, A.; Wilke, A.; Bröker, B.; Frisch, J.; Amsalem, P.; Vollmer, A.; Opitz, A.; Koch, N.; et al. High fill factor and open circuit voltage in organic photovoltaic cells with diindenoperylene as donor material. *Adv. Funct. Mater.* **2010**, *20* (24), 4295-4303.
61. Sims, L.; Hörmann, U.; Hanfland, R.; MacKenzie, R. C. I.; Kogler, F. R.; Steim, R.; Brütting, W.; Schilinsky, P. Investigation of the s-shape caused by the hole selective layer in bulk heterojunction solar cells. *Org. Electron.* **2014**, *15* (11), 2862-2867.
62. Santbergen, R.; Meguro, T.; Suezaki, T.; Koizumi, G.; Yamamoto, K.; Zeman, M. GenPro4 optical model for solar cell simulation and its application to multijunction solar cells. *IEEE Journal of Photovoltaics* **2017**, *7* (3), 919-926.
63. Shi, J.; Qin, X. R. Flux dependence of the morphology of a tetracene film on hydrogen-passivated Si(100). *Phys. Rev. B* **2006**, *73* (12), 121303.
64. Angermann, H.; Dittrich, T.; Flietner, H. Investigation of native-oxide growth on HF-treated Si(111) surfaces by measuring the surface-state distribution. *Appl. Phys. A* **1994**, *59* (2), 193-197.
65. Rauscher, S.; Dittrich, T.; Aggour, M.; Rappich, J.; Flietner, H.; Lewerenz, H. J. Reduced interface state density after photocurrent oscillations and electrochemical hydrogenation of n-Si(111): A surface photovoltage investigation. *Appl. Phys. Lett.* **1995**, *66* (22), 3018-3020.
66. Rappich, J.; Dittrich, T. Chapter 1 - Electrochemical passivation of Si and SiGe surfaces. In *Handbook of Thin Films*, Singh Nalwa, H., Ed. Academic Press: Burlington, 2002; pp 1-56.
67. Tritsch, J. R.; Chan, W.-L.; Wu, X.; Monahan, N. R.; Zhu, X. Y. Harvesting singlet fission for solar energy conversion via triplet energy transfer. *Nat. Comm.* **2013**, *4* (1), 2679.
68. Zhu, X. Y. How to draw energy level diagrams in excitonic solar cells. *J. Phys. Chem. Lett.* **2014**, *5* (13), 2283-2288.
69. Kahn, A.; Koch, N.; Gao, W. Electronic structure and electrical properties of interfaces between metals and  $\pi$ -conjugated molecular films. *J. Polym. Sci., Part B: Polym. Phys.* **2003**, *41* (21), 2529-2548.
70. Olthof, S.; Mehraeen, S.; Mohapatra, S. K.; Barlow, S.; Coropceanu, V.; Brédas, J.-L.; Marder, S. R.; Kahn, A. Ultralow doping in organic semiconductors: Evidence of trap filling. *Phys. Rev. Lett.* **2012**, *109*, 176601.

71. Schultz, T.; Niederhausen, J.; Schlesinger, R.; Sadofev, S.; Koch, N. Impact of surface states and bulk doping level on hybrid inorganic/organic semiconductor interface energy levels. *J. Appl. Phys.* **2018**, *123* (24), 245501.
72. Wang, R.; Wang, Y.; Wu, C.; Zhai, T.; Yang, J.; Sun, B.; Duhm, S.; Koch, N. Direct observation of conductive polymer induced inversion layer in n-Si and correlation to solar cell performance. *Adv. Funct. Mater.* **2020**, *30* (4), 1903440.
73. Gleason-Rohrer, D. C.; Brunschwig, B. S.; Lewis, N. S. Measurement of the band bending and surface dipole at chemically functionalized Si(111)/vacuum interfaces. *J. Phys. Chem. C* **2013**, *117* (35), 18031-18042.
74. Panda, A.; Renshaw, C. K.; Oskooi, A.; Lee, K.; Forrest, S. R. Excited state and charge dynamics of hybrid organic/inorganic heterojunctions. II. Experiment. *Phys. Rev. B* **2014**, *90* (4), 045303.
75. Renshaw, C. K.; Forrest, S. R. Excited state and charge dynamics of hybrid organic/inorganic heterojunctions. I. Theory. *Phys. Rev. B* **2014**, *90* (4), 045302.
76. Bender, J. A.; Raulerson, E. K.; Li, X.; Goldzak, T.; Xia, P.; Van Voorhis, T.; Tang, M. L.; Roberts, S. T. Surface states mediate triplet energy transfer in nanocrystal–acene composite systems. *J. Am. Chem. Soc.* **2018**, *140* (24), 7543-7553.
77. Bäessler, H.; Köhler, A. “Hot or cold”: how do charge transfer states at the donor–acceptor interface of an organic solar cell dissociate? *Phys. Chem. Chem. Phys.* **2015**, *17*, 28451-28462.
78. Durrant, J. R.; Haque, S. A.; Palomares, E. Photochemical energy conversion: from molecular dyads to solar cells. *Chem. Commun.* **2006**, 3279-3289.
79. Köhler, A.; Bäessler, H. What controls triplet exciton transfer in organic semiconductors? *J. Mater. Chem.* **2011**, *21*, 4003-4011.
80. Li, X.; Tang, M. L. Triplet transport in thin films: fundamentals and applications. *Chem. Commun.* **2017**, *53*, 4429-4440.
81. Piland, G. B.; Bardeen, C. J. How morphology affects singlet fission in crystalline tetracene. *J. Phys. Chem. Lett.* **2015**, *6* (10), 1841-1846.
82. Langner, A.; Su, Y.; Sokolowski, M. Luminescence quenching of tetracene films adsorbed on an ultrathin alumina AlO<sub>x</sub> layer on Ni<sub>3</sub>Al(111). *Phys. Rev. B* **2006**, *74*, 045428.
83. Liu, X.; Zhan, Y.; Braun, S.; Li, F.; Fahlman, M. Interfacial electronic properties of pentacene tuned by a molecular monolayer of C60. *Phys. Rev. B* **2009**, *80* (11), 115401.
84. Döring, R. C.; Rosemann, N. W.; Huttner, A.; Breuer, T.; Witte, G.; Chatterjee, S. Charge-transfer processes and carrier dynamics at the pentacene—C60 interface. *J. Phys.: Condens. Matter* **2019**, *31* (13), 134001.
85. Dumas, P.; Gruyters, M.; Rudolf, P.; He, Y.; Yu, L. M.; Gensterblum, G.; Caudano, R.; Chabal, Y. J. Vibrational study of C60 overlayers on H-Si(111)-(1 × 1). *Surf. Sci.* **1996**, *368* (1), 330-336.
86. Fujikawa, Y.; Sadowski, J. T.; Kelly, K. F.; Nakayama, K. S.; Nagao, T.; Sakurai, T. Fluorine etching on the Si(111)-7×7 surfaces using fluorinated fullerene. *Surf. Sci.* **2002**, *521* (1), 43-48.
87. Wang, X.; Esfarjani, K.; Zebarjadi, M. First-principles calculation of charge transfer at the silicon–organic interface. *J. Phys. Chem. C* **2017**, *121* (29), 15529-15537.
88. Akaike, K.; Nardi, M. V.; Oehzelt, M.; Frisch, J.; Opitz, A.; Christodoulou, C.; Ligorio, G.; Beyer, P.; Timpel, M.; Pis, I.; et al. Effective work function reduction of practical electrodes using an organometallic dimer. *Adv. Funct. Mater.* **2016**, *26* (15), 2493-2502.
89. Schultz, T.; Schlesinger, R.; Niederhausen, J.; Henneberger, F.; Sadofev, S.; Blumstengel, S.; Vollmer, A.; Bussolotti, F.; Yang, J.-P.; Kera, S.; et al. Tuning the work function of GaN with organic molecular acceptors. *Phys. Rev. B* **2016**, *93*, 125309.

TOC figure

